INSTITUTE OF PHYSICS PUBLISHING JOURNAL OF MICROMECHANICS AND MICROENGINEERING

J. Micromech. Microeng. **14** (2004) 226–234 PII: S0960-1317(04)61251-4

# Large-force electrothermal linear micromotors

**John M Maloney**[1], **David S Schreiber and Don L DeVoe**

Center for Micro Engineering, Department of Mechanical Engineering and Institute for Systems Research, University of Maryland at College Park, College Park, MD 20742, USA

E-mail: john@maloney.org

Received 21 March 2003, in final form 15 September 2003
Published 17 November 2003
Online at stacks.iop.org/JMM/14/226 (DOI: 10.1088/0960-1317/14/2/009)

**Abstract**

Electrothermal linear micromotors fabricated by deep reactive ion etching of silicon-on-insulator wafers are presented. These high-aspect-ratio motors are powered by thermal actuator arrays with a height of 50 $\mu$m. Synchronized arrays, each containing ten actuators connected by a midpoint yoke, are used to advance a slider through frictional contact. Forces of 6.7 mN have been demonstrated at a voltage of 12 V using motors measuring 2.5 mm by 2.1 mm. Unidirectional motors have been successfully operated at speeds of up to 1 mm $s^{-1}$ over a range in excess of 2 mm. Motors are found to be well suited for positioning compliant mechanisms and similar applications requiring large forces and displacements at low drive voltages.

## 1. Introduction

Micromachined linear motors have been demonstrated in which the repetition of small actuator deflections is used to move a slider through a large range of linear motion [1–8]. These motors find application in areas such as component positioning, microassembly and robotics. In table 1 a variety of micromachined linear motors is listed that have been characterized. In theory, the slider length and range of motion are unlimited for these inchworm/stepper configurations. However, friction and out-of-plane bowing present practical limits [5]. In the motors described in the literature, sliders are frequently run to the limit of their fabricated length.

Micromachined linear motors typically contain arrays of electrostatic or electrothermal actuators. For example, pairs of orthogonal electrostatic comb drives have been used to move an impact head in contact with a slider and subsequently push the slider forward [2, 6]. These electrostatic motors feature relatively high energy efficiency, as high as 8% as reported by Yeh *et al* [6]. However, voltages in excess of 30 V are frequently required to obtain any significant displacement, and force output so far has been limited to well below 1 mN. Electrothermal motors have been operated at voltages under 12 V, and as low as 1.2 V by Park *et al* [3–5, 7]. Relatively large forces can be produced due to the large energy density of thermal actuators. A significant disadvantage of these motors is their low efficiency, limiting use to high-power applications.

There are several ways that actuators can interact with sliders to produce motion. In the vibromotor approach, sliders are displaced by momentum transfer in a series of impacts [1, 4]. Ideally, actuators are run at their natural resonant frequency to maximize displacement and impact momentum. Although vibromotors cannot sustain significant opposing forces during operation, they have been successfully used for low-friction component positioning.

A second method of slider contact has been demonstrated by using impact heads and sliders with notched edges, which greatly enhance grip [3, 5–7]. Notched edges increase the amount of force that can be transmitted to a slider, and forces exceeding 200 $\mu$N have been demonstrated by both electrothermal and electrostatic motors [5, 6]. The positioning resolution of these motors is ultimately limited to the minimum distance between notches, which is determined by fabrication design rules.

In the third method, the slider is held and advanced solely due to frictional contact between the impact heads and the slider [2, 8]. A large amount of actuator force is required to grip the slider tightly against opposing forces. Frictional motors offer the opportunity for improved ultimate positioning resolution, which is limited by sidewall roughness only. A disadvantage of these motors is the possibility of slip during

[1] Present address: MicroCHIPS, Inc., 6-B Preston Court, Bedford, MA 01730, USA.

  

**Table 1.** Fully micromachined linear motors (inchworm/stepper configurations).

| Group | Mechanism | Contact method | Material (height) | Force | Cycle frequency | Speed | Demonstrated range | Voltage (V) | Size |
|---|---|---|---|---|---|---|---|---|---|
| Daneman *et al* [1] | Electrostatic | Impact | PolySi (4 $\mu$m) | >2.5 $\mu$N | 7.0–7.2 kHz | >1 mm s$^{-1}$ | >350 $\mu$m | 62.5 | |
| Baltzer *et al* [2] | Electrostatic | Friction | PolySi (1.8 $\mu$m) | >1 $\mu$N | | | 110 $\mu$m | Up to 40 | 1.8 mm × 1.5 mm |
| Pai *et al* [4] | Electrothermal | Impact, friction | PolySi (2 $\mu$m) | | 10.5 kHz | 10.2 mm s$^{-1}$ | 390 $\mu$m | 12 | |
| Park *et al* [5] | Electrothermal | Notch | Ni (11 $\mu$m) | 204 $\mu$N | 24 ms pulse | | 104 $\mu$m | 1.2 | |
| Yeh *et al* [6] | Electrostatic | Notch | Si (50 $\mu$m) | 260 $\mu$N | 1 kHz | 4 mm s$^{-1}$ | 80 $\mu$m | 33 | 3 mm × 1 mm |
| Kwon *et al* [7] | Electrothermal | Notch | Si (40 $\mu$m) | 57 $\mu$N | 250 Hz | 0.4 mm s$^{-1}$ | | Up to 13.5 | |
| Tas *et al* [8] | Electrostatic | Friction | PolySi (5.3 $\mu$m) | 3 $\mu$N | 1 Hz | | 15 $\mu$m | 40 | |
| This work | Electrothermal | Friction | Si (50 $\mu$m) | 6.7 mN | 80 Hz | 1 mm s$^{-1}$ | >2 mm | 12 | 2.5 mm × 2.1 mm |

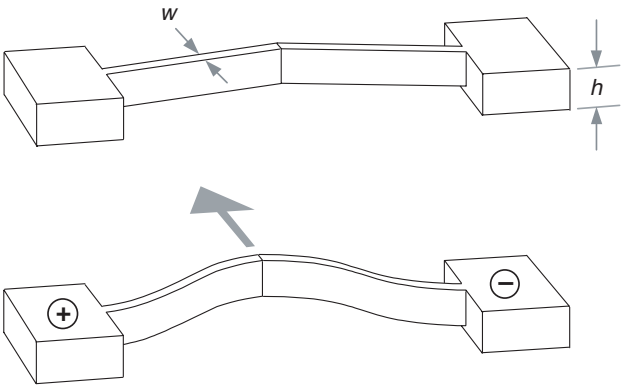


**Figure 1.** Conceptual view of high-aspect-ratio actuator used in electrothermal linear motor, as fabricated and in operation under an applied current.

operation [6]. For precise positioning, a closed-loop system with displacement-sensing capability would be required.

In this paper, we present large-force frictional motors using arrays of high-aspect-ratio electrothermal actuators. It is a goal of this work to demonstrate motors for positioning compliant mechanisms requiring displacements of hundreds of microns and forces in excess of 1 mN. An actuator type well suited for this application is the V-beam, or bent-beam, electrothermal actuator [9–13]. This actuator, illustrated in figure 1, consists of a clamped–clamped beam undergoing heat generation from an applied current. Deflection occurs parallel to the substrate, and the beam is offset slightly at the midpoint to control the direction of motion. Unlike bimorph-type thermal actuators, these actuators produce only translational motion and are therefore suitable for arrays in which a yoke passes through the midpoint [12]. Multiple actuators that share anchors are effectively wired in parallel to produce increased force without loss of deflection.

Deep reactive ion etching (DRIE) of silicon-on-insulator (SOI) wafers offers a simple way to fabricate high-aspect-ratio devices in single crystal silicon. We have fabricated motors using SOI/DRIE technology and characterized motor force, speed, displacement, efficiency and frequency response. We also present a transient model for predicting the frequency response of high-aspect-ratio thermal actuators. Although not demonstrated in this work, the use of frictional contact is intended to improve positioning resolution against large opposing forces by eliminating the constraint of notched sliders.

## 2. Motor design and operation

A schematic of a high-aspect-ratio electrothermal linear motor is shown in figure 2. This motor uses two pairs of actuator arrays to alternately advance and clamp a slider against an opposing force; each pair consists of an array of ten V-beam actuators on each side of the slider. Because the actuators advance the slider through frictional contact, the impact heads tend to pull the slider back when power is removed. Therefore, it is necessary to clamp the slider between cycles. The most efficient type of clamp is an additional pair of actuator arrays that will push the slider forward when the first pair is withdrawn. This positioning scheme is illustrated in figure 3, in which two synchronized, dc-biased square waves are used to control the two pairs of actuator arrays.

The essential idea behind motor operation is that the compliant yokes enforce one-way motion when an impact head is in contact with the slider. While forward-pointing impact heads are pushed against the slider, the force required to move the slider forward is much less than the force required to move it in reverse. In effect, a ratcheting mechanism is created through frictional contact. As shown in figure 3, the actuators are initially biased at 12 V to a position of maximum deflection, which advances the slider the distance of one step. This voltage was chosen to provide the largest possible deflection without entering the intrinsic region in the silicon beam, an unstable operating point for voltage-controlled thermal actuators [11]. Slider motion is achieved by using alternate, synchronized −2 V pulses. During each pulse, one pair of impact heads pulls back slightly but remains in contact with the slider due to the 10 V bias. The large frictional force maintained by the second pair of impact heads prevents the slider from being pulled back. When the pulse ends, the first pair moves forward again. This motion advances the slider, which slips by the second pair with relatively low friction. As long as sufficient

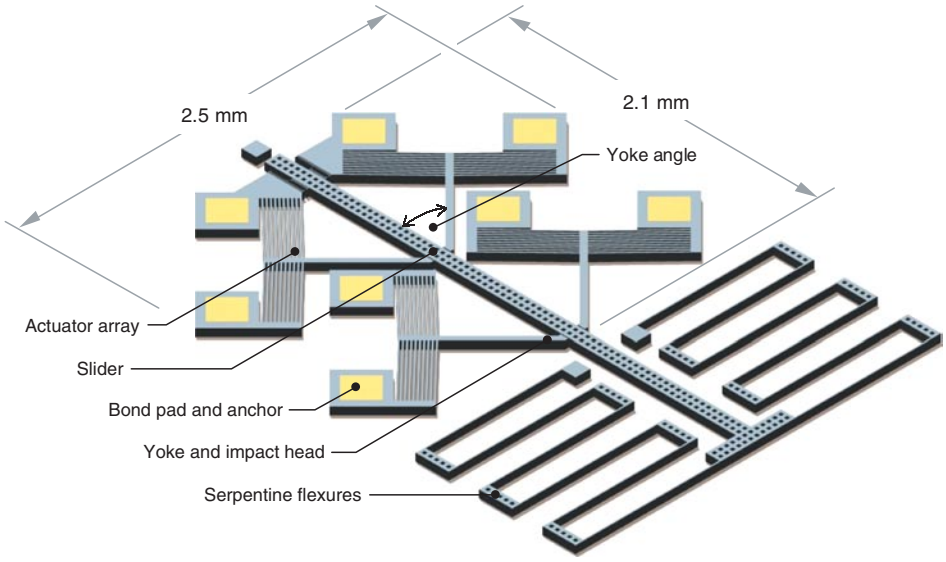


**Figure 2.** Schematic of unidirectional linear motor with serpentine flexures used to evaluate motor efficiency.

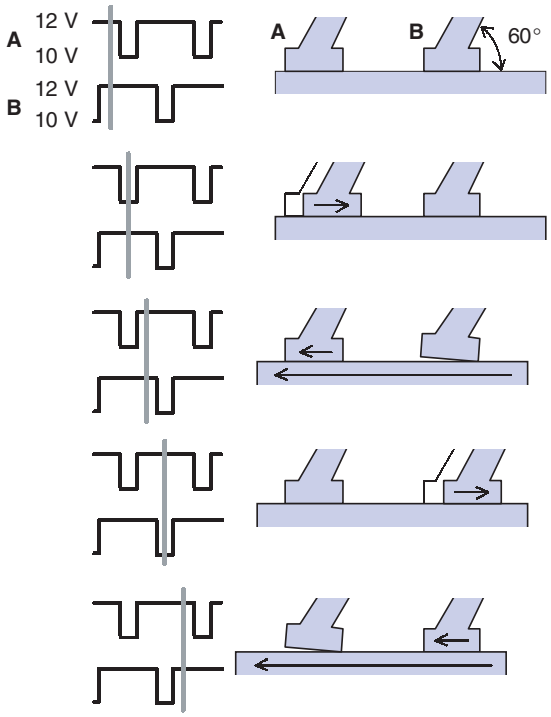


**Figure 3.** Sequence of motor operation. Yoke angles of 60° are shown.

voltage is applied, the impact heads remain in contact with the slider. The resulting frictional contact is sufficient to maintain deflection against large opposing forces.

Following an optimization study of actuator dimensions, we chose to use actuators with a width of 10 $\mu$m, an offset of 10 $\mu$m, a length of 1000 $\mu$m and a spacing of 10 $\mu$m. In general, actuator deflection increases with decreasing width and offset and increasing length; these dimensions were chosen to provide deflections of at least 10 $\mu$m while keeping the total motor size around 5 mm$^2$. The resulting unidirectional motor design measures 2.5 mm by 2.1 mm, including bond pads. To evaluate the effect of varying yoke angle and width, yokes were fabricated with angles of 45° and 60° and widths of 10, 20, 30 and 40 $\mu$m. Angles are measured as shown in figure 2. For each angle, the shortest possible yoke length was used to reduce motor size; the resulting lengths for 45° and 60° yokes are about 600 and 350 $\mu$m, respectively. The impact heads are 50 $\mu$m long.

Motors were designed in three configurations. In the first configuration, shown in figure 2, low-stiffness serpentine flexures are attached to the slider so that efficiency can be calculated from a simultaneous measurement of force and speed. The second configuration includes high-stiffness folded flexures so that motor force can be determined. The third configuration uses an unrestrained slider to demonstrate speed and range. This slider is held in place during the release step by thin support beams that are broken off with a probe tip prior to testing.

## 3. Motor fabrication

The motors were fabricated on a SOI wafer by DRIE. The wafer consists of a 50 $\mu$m active layer of highly doped single crystal silicon separated from a silicon substrate by 2 $\mu$m of silicon dioxide. The resistivity of the active layer at room temperature was measured at 0.0133 Ω cm by four-point probe. For p-doped silicon, this resistivity corresponds to a dopant concentration of approximately $10^{19}$ cm$^{-3}$ [14].

Two photomasks were used during fabrication. First, a 5 nm Cr/350 nm Au layer was deposited by thermal evaporation and patterned by lithography and wet etching to define bond pads. Photoresist was then patterned to define the silicon structures, and DRIE was used to etch completely through the active layer, stopping on the buried oxide. After stripping the photoresist, the wafer was diced and devices were released by placing the chips in 49% hydrofluoric acid (HF) for 18 min. Although HF etches chromium, the 5 nm adhesion layer was sufficiently thin to resist attack during the release step because of mass transport limitations. Previous designs used an adhesion layer thickness of 20 nm, but the gold bond

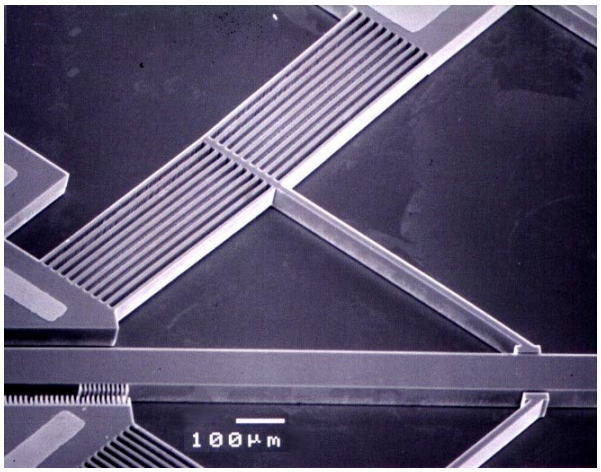


**Figure 4.** Micrograph of fabricated actuator array connected by midpoint yoke.

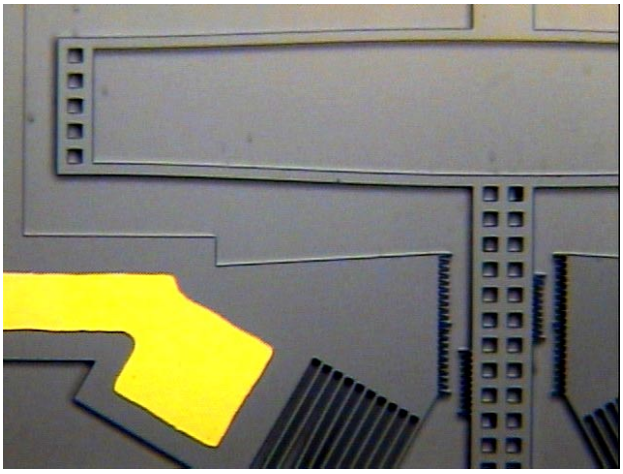

**Figure 5.** Photograph of folded flexures during force testing. The edges of a pair of actuator arrays are visible at bottom. The Vernier scale shows a displacement of 28 $\mu$m, corresponding to a force of 6.3 mN.

pads were found to delaminate from the silicon during HF etching. After the release step, the chips were rinsed with DI water and isopropanol and dried with nitrogen. A micrograph of one of the fabricated actuator arrays is shown in figure 4.

We found the fabricated feature width to be slightly smaller than the design width. Because the room temperature resistivity of the silicon is known, the average fabricated width $w$ can be calculated by using the equation

$$w = \frac{\rho L}{Rh} \tag{1}$$

where $\rho$ is the resistivity and $R$ is the measured resistance of a test beam. It was found with this method that beam width was typically reduced 1.5 to 2.5 $\mu$m from design width; this estimate was supported by SEM measurements. For the calculations performed in this paper, fabricated beam width is assumed to be 2 $\mu$m less than design width. For example, the serpentine folded flexure design width of 10 $\mu$m is assumed to be reduced to 8 $\mu$m.

The use of DRIE on SOI wafers offers several advantages when fabricating single-layer devices. First, DRIE of single crystal silicon allows robust devices to be constructed. Large aspect-ratios and low stress gradients reduce the possibility of stiction or bowing during device release and operation. Second, device height is not limited by the constraints of surface micromachining processes. Rather, by choosing a certain active layer thickness, motors can be fabricated that will produce appropriate forces for a specific application. Third, customized SOI wafers contain a doped, releasable mechanical layer, which simplifies the fabrication process. These advantages may be offset, however, by the higher cost of SOI wafers, which can be an order of magnitude more expensive than standard silicon wafers.

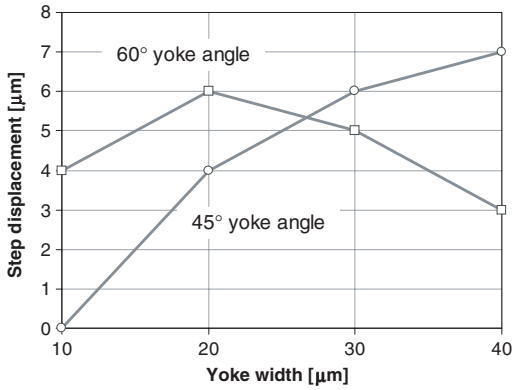


**Figure 6.** Displacement for one actuator step versus yoke width and angle.

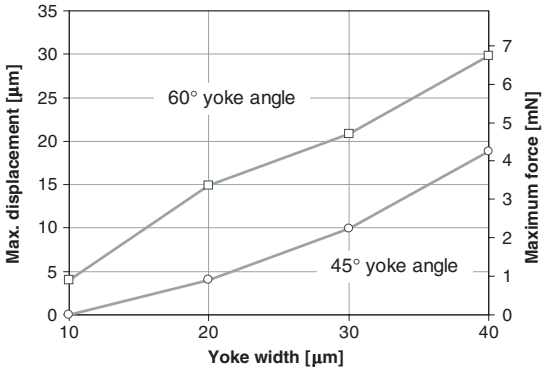


**Figure 7.** Maximum displacement (left axis) and corresponding force (right axis) versus yoke width and angle. Forces are calculated using the spring constant of the folded flexures.

## 4. Experimental results

### *4.1. Motor force and efficiency*

One motor configuration, pictured in figure 5, employs folded flexures at the end of the slider to allow motor force to be evaluated for different yoke geometries. In the picture, the slider has been displaced 28 $\mu$m downward against an opposing force created by the folded flexures. Vernier scales with a resolution of $\pm 0.5$ $\mu$m are fabricated on the slider and anchors to measure deflection.

Displacement and force data are presented in figures 6 and 7 for motors with varying yoke angle and width. The input voltage and current were 12 V and approximately 70 mA per array, or 7 mA per actuator. The folded flexures are 600 $\mu$m long and have a fabricated width of 18 $\mu$m (design width of 20 $\mu$m), resulting in a spring constant of 224 N m$^{-1}$. This value is used to determine the force corresponding to a certain displacement and is calculated using a Young's modulus for single crystal silicon of 166 GPa.

The step displacement is shown in figure 6, representing the slider displacement when a single pair of arrays is actuated. The zero value for the 10 $\mu$m, 45° yoke indicates that the impact heads slid against the slider, failing to move it at all. This yoke was the most compliant of those tested. The impact heads on the other yokes were able to move the sliders forward without any slipping. An optimal beam width that maximizes step displacement is observed at 20 $\mu$m for 60° yokes. The corresponding width for 45° yokes is at least 40 $\mu$m.

Shown in figure 7 are the maximum displacement and corresponding force values. These values represent the maximum displacement attainable by alternating between two pairs of actuator arrays for one or more steps; this displacement is recorded at the point where the impact heads begin to slide. At this point, frictional contact is no longer sufficient to move the slider forward against the opposing force created by the flexures.

The individual actuator force can be estimated by examining the yoke geometry. For example, the 6.7 mN force demonstrated with 60°/40 $\mu$m yokes corresponds to a 6.7 mN force per actuator array, or 0.67 mN per actuator:

$$\frac{6.7\,\text{mN}}{20\cos 60^\circ} = 0.67\,\text{mN}. \tag{2}$$

For simplicity, we neglect the change in yoke angle during operation. By trigonometry, the normal and frictional forces exerted by each impact head on the slider are calculated to be 5.8 and 3.4 mN, respectively.

An increase in sustainable force with yoke width was observed due to the increase in yoke stiffness. The 60° yokes consistently produced more force than the 45° yokes; however, the 45°/40 $\mu$m yokes produced the most favorable combination of step displacement and maximum force (7 $\mu$m and 4.3 mN) for our application. This yoke configuration was selected for evaluating motor efficiency and speed.

Motor output power and efficiency is calculated using the configuration, shown in figures 2 and 8, that employs serpentine flexures to create a low-stiffness spring. The mechanical work done by a motor connected to flexures is the product of the final displacement and average force, and the corresponding power can be obtained by dividing the work done by the required positioning time. For a motor starting at a neutral position with no opposing forces, output power is

$$P = \frac{Fd}{2t} = \frac{kd^2}{2t} \tag{3}$$

where $F$ is the final opposing force and $k$ is the stiffness of the serpentine flexures, which contain 12 arms that are 900 $\mu$m long and have a fabricated width of 8 $\mu$m (design width of 10 $\mu$m). The spring constant $k$ is calculated to be 1.94 N m$^{-1}$.

The slider shown in figure 8 was positioned by two pairs of actuator arrays (45°/40 $\mu$m yokes) driven by synchronized 80 Hz signals. A maximum displacement of 570 $\mu$m was achieved after 1 s; the output power and power density were therefore found to be 0.315 $\mu$W and 1201 W m$^{-3}$, respectively. For an input power of about 3 W, the motor efficiency is only $10^{-7}$, compared to 0.08 for a recently demonstrated electrostatic motor [6]. It should be noted, however, that the power requirements may be reduced by incorporating the passive locks demonstrated by Park *et al* [5].

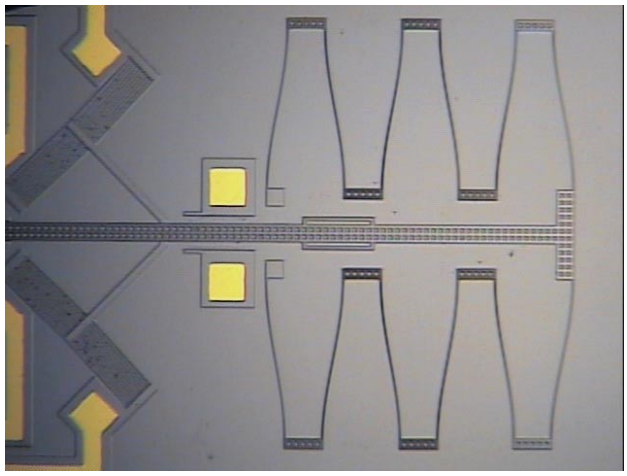

**Figure 8.** Photograph of serpentine flexures during efficiency testing. A pair of actuator arrays is visible at left. The slider is displaced 570 $\mu$m.

**Table 2.** Parameters of transient heat transfer analysis.

| Parameter | | Value |
|---|---|---|
| $c$ | Specific heat, silicon (298–800 K) | 700–885 J (kg K)$^{-1}$ |
| $g$ | Gap between beam and substrate | 2 $\mu$m |
| $h$ | Beam height | 50 $\mu$m |
| $k_a$ | Thermal conductivity, air | 0.03 W (m K)$^{-1}$ |
| $k_s$ | Thermal conductivity, silicon (298–800 K) | 148–42 W (m K)$^{-1}$ |
| $p$ | Density, silicon | 2330 kg m$^{-3}$ |
| $S$ | Conduction shape factor | 2.5 |
| $\rho$ | Resistivity, silicon (room temperature) | 0.0133 Ω cm |

### *4.2. Frequency response*

Models describing the combined electrothermal and thermomechanical behavior of actuators, including the effects of temperature-dependent material properties, have previously been developed [11–13, 15–18]. In this section, a transient model is introduced and actuator and motor frequency response are presented. The parameters for the transient analysis are listed in table 2. Due to the SOI wafer configuration, the height $h$ of the beams corresponds to the active layer thickness, and the gap $g$ between the beams and the substrate corresponds to the oxide layer thickness. Some material properties are given in the form of ranges, corresponding to the change in their values across a given temperature range. The impact of this temperature dependence will be discussed later in this section.

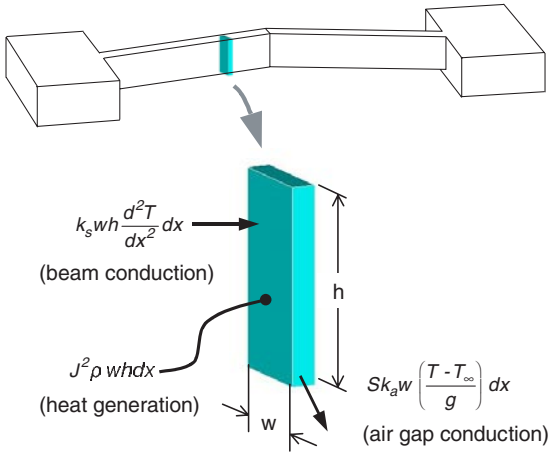


**Figure 9.** Differential element of actuator showing heat generation and heat loss terms.

Because actuator length is substantially larger than height or width, we use a 1D differential element to model the temperature distribution in the silicon [19]. This element, with height $h$, width $w$ and thickness d$x$, is illustrated in figure 9, in which $J$ represents the current per unit area through the element. The conduction shape factor $S$ represents the ratio of conduction heat loss from the sides and bottom of the beam to expected heat loss from the bottom of the beam only [19]. From finite element analysis of the actuators used in this work, the value of $S$ is estimated to be 2.5 [11].

It has been shown that, in the case of a very small gap under a suspended beam, convection and radiation can be considered to be negligible and conduction through air to the substrate dominates [15, 17, 18]. For example, Hickey *et al* calculated the Rayleigh and Nusselt numbers associated with natural convection from a suspended beam with a characteristic size of 2 $\mu$m and estimated a convection coefficient of approximately 100 W (m$^2$ K)$^{-1}$ [17]. The convection coefficient $h_c$ was further shown to decrease with increasing characteristic size $S_c$ as $h_c \sim {S_c}^{-1/4}$ [17, 20]. By using a characteristic size of 50 $\mu$m, corresponding to actuator height, we obtain a convection coefficient of approximately 45 W (m$^2$ K)$^{-1}$. The convection heat loss (per unit length and temperature rise) from the differential element shown in figure 9 is estimated to be $2h_c(h + w) = 0.0052$ W (m K)$^{-1}$, much smaller than the heat loss from air conduction ($Sk_a w/g = 0.3$ W (m K)$^{-1}$). Convection effects are therefore assumed to be negligible in this analysis.

The transient heat equation can be written as,

$$k_s \frac{\mathrm{d}^2T(x,t)}{\mathrm{d}x^2} + J^2\rho - Sk_a\frac{T(x,t)-T_\infty}{gh} = cp\frac{\mathrm{d}T(x,t)}{\mathrm{d}t}. \tag{4}$$

The corresponding time-dependent equation and boundary conditions are

$$\frac{\mathrm{d}\phi(x,t)}{\mathrm{d}t} = \frac{k_s}{cp}\frac{\mathrm{d}^2\phi(x,t)}{\mathrm{d}x^2} + \frac{J^2\rho}{cp}\,\mathrm{e}^{\beta t} \tag{5}$$

$$\phi(0,t) = \phi(L,t) = \phi(x,0) = 0 \tag{6}$$

where $L$ represents the length of the beam, and the following variable substitutions have been made:

$$\phi(x,t) = [T(x,t) - T_\infty]\,\mathrm{e}^{\beta t} \tag{7}$$

$$\beta = \frac{Sk_a}{ghcp}. \tag{8}$$

We now justify the use of a room-temperature boundary condition on both ends of the beam. The maximum power dissipated by a single actuator during operation is approximately 0.2 W. By examining the worst-case scenario where this heat is dissipated entirely to the substrate through the two 600 $\times$ 600 $\mu$m$^2$ silicon anchors, a heat flux of 0.28 MW m$^{-2}$ is obtained. Because the anchors are separated from the silicon substrate by a 2 $\mu$m layer of silicon dioxide with thermal conductivity 1.4 W (m K)$^{-1}$, it is calculated that the temperature rise in the anchors during operation is approximately 0.4 °C. The anchors are therefore assumed to remain at ambient temperature.

The general solution to equation (5) is

$$T(x,t) = T_\infty + \sum_{n=1}^{\infty}\frac{\zeta_n}{\gamma_n+\beta}[1-\mathrm{e}^{-(\gamma_n+\beta)t}]\sin\left(\frac{n\pi x}{L}\right) \tag{9}$$

where

$$\gamma_n = \left(\frac{n\pi}{L}\right)^2\frac{k_s}{cp} \tag{10}$$

$$\zeta_n = \frac{2J^2\rho}{cpn\pi}[1-\cos(n\pi)]. \tag{11}$$

This solution implies a first-mode time constant of

$$\tau_1 = (\gamma_1+\beta)^{-1} = \left(\frac{\pi^2 k_s}{cpL^2} + \frac{Sk_a}{ghcp}\right)^{-1} \tag{12}$$

which offers a useful way of comparing heat loss contributions from silicon conduction and air conduction. The first term represents heat loss through the beam to the anchors, and the second term represents heat loss through the air gap to the substrate.

Between 298 and 800 K, the thermal conductivity of single crystal silicon decreases from 148 to 42 W (m K)$^{-1}$ and the specific heat of silicon increases from 700 to 885 J (kg K)$^{-1}$ [21]. The upper value of 800 K corresponds to the estimated maximum temperature in the actuators during normal operation, found by comparing the average silicon resistivity of an actuator beam to the temperature-dependent resistivity of p-doped silicon. An example of this measurement is shown in figure 10, in which actuator displacement is also plotted. The estimated dopant concentration of the single crystal silicon used in this work, $10^{19}$ cm$^{-3}$, corresponds to an intrinsic temperature of approximately 1000 K [22]. At this temperature, intrinsic and dopant carrier concentrations are equal and the resistivity is at a maximum. Due to a thermal runaway effect when the temperature coefficient of resistivity becomes negative, the intrinsic temperature dictates the approximate maximum operating power for voltage-controlled devices. Although temperatures along the beam are expected to vary from room temperature to up to 1000 K, the 800 K value is useful as an upper bound for estimating the change in device response due to temperature-dependent material properties. We note that, because of these variations

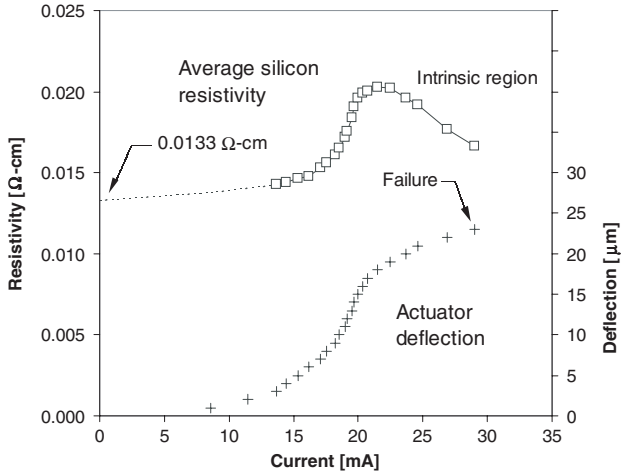


**Figure 10.** Average resistivity of p-doped silicon actuator beam (left axis) and measured actuator deflection (right axis) versus current.

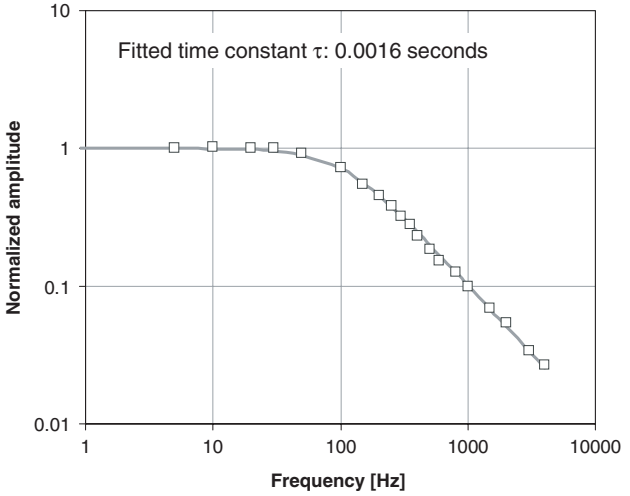


**Figure 11.** Normalized amplitude versus frequency for individual V-beam actuator.

in temperature, the maximum average resistivity in the beam does not occur precisely at the intrinsic point.

Using equation (12) with material property values at 298 and 800 K, the first-mode time constant of a 1000 $\mu$m long actuator is expected to lie approximately between 0.8 and 1.8 ms. A temperature-independent value of 0.03 W (m K)$^{-1}$ is used for the thermal conductivity of air in this calculation. The corresponding $-3$ dB frequencies, 207 and 112 Hz, are low compared to the $-3$ dB frequencies of low-aspect-ratio actuators with much smaller heights [4, 17]. They are also far lower than the resonant frequency, approximately 70 kHz, of a clamped–clamped beam with the same dimensions of a typical actuator. Inertial effects are therefore not expected to appear in the frequency response of single high-aspect-ratio thermal actuators.

The frequency response of a single actuator was examined with a laser Doppler vibrometer. This test was performed by mounting a chip vertically and focusing the laser on the side of the actuator beam. The normalized frequency response is shown in figure 11. As expected, the deflection is essentially frequency independent at low frequencies. As the frequency is

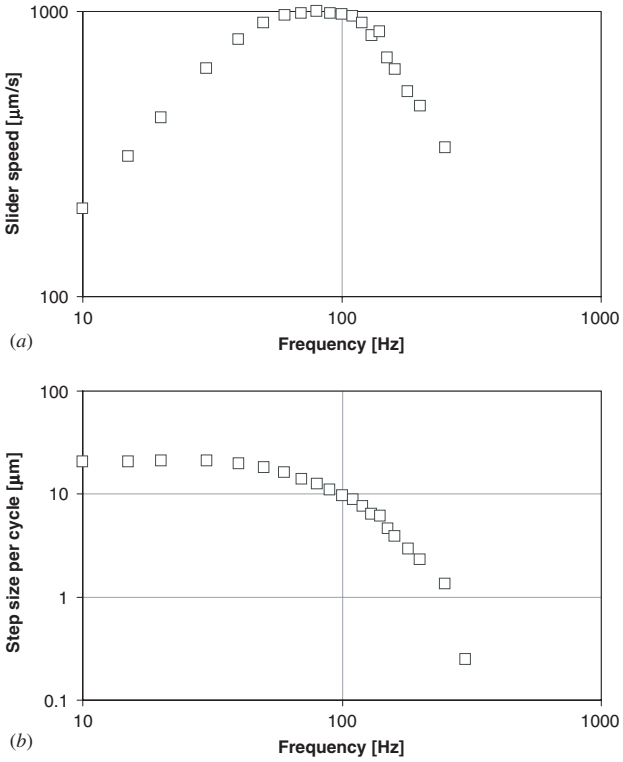


**Figure 12.** Slider speed (*a*) and step size per cycle versus frequency (*b*) for linear motor. A maximum slider speed of 1 mm s$^{-1}$ occurs at 80 Hz.

increased past 100 Hz, the displacement amplitude decreases by 20 dB per decade, which is consistent with the first-order nature of a thermal system. The time constant of this actuator is estimated at 1.6 ms by fitting a curve to the frequency response, shown as the solid line in figure 11. This value lies between the predicted first-mode time constants calculated above.

Motor speed was tested with the motor configuration featuring an unrestrained slider and 45°/40 $\mu$m yokes. During speed testing, the slider was frequently actuated over its entire usable length, in excess of 2 mm. Motor speed and step size versus frequency are plotted in figure 12. A 10-cycle input signal was used, and motor speed $v$ is calculated as

$$v = \frac{Df}{10} \tag{13}$$

where $D$ is the total displacement observed and $f$ is the driving frequency of the synchronized control signals. The operational current was less than 70 mA per actuator array, or 7 mA per actuator. The step size was calculated by dividing the displacement by 10. This step size represents the slider displacement per cycle, or twice the displacement from each pair of actuator arrays per cycle.

The maximum slider speed of 1 mm s$^{-1}$ was observed at 80 Hz. At low frequencies, the slider is advanced over 20 $\mu$m per cycle by the actuator arrays. As the frequency is increased past 100 Hz, step size decreases at a rate of more than 20 dB per decade and motor speed decreases. Unlike the displacement of a single actuator, this behavior is not indicative of a first-order system. We believe that displacement decreases at high frequencies because inertial effects from slider acceleration become significant. It is also possible that slip occurs between

the impact heads and the slider, a result of trying to accelerate the slider using only frictional contact. The possibility of slip during normal operation of these motors emphasizes the need for a closed-loop system to achieve precise positioning.

## 5. Conclusions

high-aspect-ratio V-beam thermal actuators are found to be well suited for use in linear motors. These actuators can be easily grouped in arrays to provide sufficient force to grasp a slider and move it forward through frictional contact only. The use of SOI wafers allows the active layer thickness, and therefore the motor height, to be customized for particular force and power requirements.

A study was performed on eight variations of yoke angle and width, and motors were fabricated in three configurations to test force, speed, efficiency and range. A maximum force of 6.7 mN was attained, which is at least an order of magnitude larger than previously reported electrothermal or electrostatic devices of similar size. Additionally, a speed of 1 mm $s^{-1}$ was recorded for a motor that was actuated over a range of more than 2 mm.

The maximum sustainable force of frictional linear motors is limited by slip between the impact heads and the slider. This maximum force was found to increase with yoke stiffness for yoke widths ranging from 10 to 40 $\mu$m. To maximize step displacement, an optimal yoke width of 20 $\mu$m was found for 60° yokes; the corresponding optimal width for 45° yokes is at least 40 $\mu$m. These forces were calculated by measuring the deflection of folded flexures attached to the slider. Because fabricated beams were found to be slightly narrower than the design specified, fabrication width was determined by resistance measurements so that accurate values could be used when characterizing.

Actuators were operated at less than the intrinsic temperature, which marks the point where intrinsic charge carriers outnumber dopant carriers in single crystal silicon. The intrinsic region features a negative temperature coefficient of resistivity and is an unstable operating area for voltage-controlled actuators due to thermal runaway. The measured resistance of an actuator beam during operation can be used to determine the approximate current required to reach the intrinsic region.

A transient model was described for predicting the frequency response of a suspended thermal actuator. The characteristic thermal time constant of operation is governed by conduction through the beam to the anchors and by conduction through the air gap to the substrate. By incorporating temperature-dependent material properties with upper and lower temperature bounds, a range was calculated for the first-mode time constant. The measured time constant of a single actuator was found to lie within this range.

The efficiency of a linear motor was estimated to be $10^{-7}$ by comparing output power, calculated from velocity and force measurements, to input power. Although such a low efficiency limits the use of thermal motors in portable, low-power devices, the characteristics demonstrated in this work make these motors appropriate for high-force, large-displacement applications such as positioning mechanisms with compliant links.

## Acknowledgments

This research was supported under DARPA contract DABT 63-98-10015 and NSF grant DMI-9875817. The authors gratefully acknowledge the fabrication assistance of Nolan Ballew, Tom Loughran and Brett Piekarski. DRIE was performed at the Army Research Laboratory and the Cornell Nanofabrication Facility (a member of the National Nanofabrication Users Network), which is supported under NSF grant ECS-9731293, Cornell University and industrial affiliates. Photomasks were produced by Kevin Larson, courtesy of Northrop Grumman.

## References

[1] Daneman M J, Tien N C, Solgaard O, Pisano A P, Lau K Y and Muller R S 1996 Linear microvibromotor for positioning optical components *J. Microelectromech. Syst.* **5** 159–65

[2] Baltzer M, Kraus T and Obermeier T 1997 A linear stepping actuator in surface micromachining technology for low voltages and large displacements *IEEE Conf. Solid-State Sensors and Actuators (Chicago, IL)* pp 781–4

[3] Reid J R, Bright V M and Butler J T 1998 Automated assembly of flip-up micromirrors *Sensors Actuators* A **66** 292–8

[4] Pai M and Tien N C 2000 Low voltage electrothermal vibromotor for silicon optical bench applications *Sensors Actuators* A **83** 237–43

[5] Park J-S, Chu L L, Oliver A D and Gianchandani Y B 2001 Bent-beam electrothermal actuators: II. Linear and rotary microengines *J. Microelectromech. Syst.* **10** 255–62

[6] Yeh R, Hollar S and Pister K S J 2002 Single mask, large force, and large displacement electrostatic linear inchworm motors *J. Microelectromech. Syst.* **11** 330–6

[7] Kwon H N, Jeong S H, Lee S K and Lee J H 2003 Design and characterization of a micromachined inchworm motor with thermoelastic linkage actuators *Sensors Actuators* A **103** 143–9

[8] Tas N R, Sonnenberg T, Molenaar R and Elwenspoek M 2003 Design, fabrication and testing of laterally driven electrostatic motors employing walking motion and mechanical leverage *J. Micromech. Microeng.* **13** N6–15

[9] Noworolski J M, Klaassen E H, Logan J R, Peterson K E and Maluf N I 1996 Process for in-plane and out-of-plane single-crystal-silicon thermal microactuators *Sensors Actuators* A **55** 65–9

[10] Cragun R and Howell L 1999 Linear thermomechanical microactuators *Proc. ASME IMECE (Nashville, TN)* pp 181–8

[11] Maloney J M, DeVoe D L and Schreiber D S 2000 Analysis and design of electrothermal actuators fabricated from single crystal silicon *Proc. ASME IMECE (Orlando, FL)* pp 233–40

[12] Que L, Park J-S and Gianchandani Y B 2001 Bent-beam electrothermal actuators: I. Single beam and cascaded devices *J. Microelectromech. Syst.* **10** 247–54

[13] Lott C. D, McLain T W, Harb J N and Howell L L 2002 Modeling the thermal behavior of a surface-micromachined linear-displacement thermomechanical microactuator *Sensors Actuators* A **101** 239–50

[14] Jaeger R C 1988 *Introduction to Microelectronic Fabrication* (Reading, MA: Addison-Wesley)

[15] Huang Q-A and Lee N K S 1999 Analysis and design of polysilicon thermal flexure actuator *J. Micromech. Microeng.* **9** 64–70

[16] Mankame N D and Ananthasuresh G K 2001 Comprehensive thermal modelling and characterization of an electro-thermal-compliant microactuator *J. Micromech. Microeng.* **11** 452–62
[17] Hickey R, Sameoto D, Hubbard T and Kujath M 2003 Time and frequency response of two-arm micromachined thermal actuators *J. Micromech. Microeng.* **13** 40–6
[18] Geisberger A A, Sarkar N, Ellis M and Skidmore G D 2003 Electrothermal properties and modeling of polysilicon microthermal actuators *J. Microelectromech. Syst.* **12** 513–23
[19] Lin L and Chiao M 1996 Electrothermal responses of lineshape microstructures *Sensors Actuators* A **55** 35–41
[20] Incropera F and DeWitt D 1996 *Fundamentals of Heat and Mass Transfer* (New York: Wiley)
[21] Touloukian Y S, Powell R W, Ho C Y and Klemens P G 1970 *Thermophysical Properties of Matter* (New York: IFI/Plenum)
[22] Pearson G L and Bardeen J 1949 Electrical properties of pure silicon and silicon alloys containing boron and phosphorus *Phys. Rev.* **75** 865–83